Journal of The Electrochemical Society, **152** (6) A1290-A1300 (2005)
0013-4651/2005/152(6)/A1290/11/$7.00 © The Electrochemical Society, Inc.

Analytical and Numerical Analysis of PEM Fuel Cell Performance Curves

A. A. Kulikovsky,[a,c,*,z] T. Wüster,[a,b] A. Egmen,[a] and D. Stolten[a]

[a]*Institute for Materials and Processes in Energy Systems, Research Center "Jülich," D-52428 Jülich, Germany*
[b]*RWTH Aachen, 52056 Aachen, Germany*

We present a novel approach for analyzing the experimental voltage-current curves of a polymer electrolyte membrane (PEM) fuel cell. State-of-the-art numerical models involve many poorly known parameters. This makes a comparison of numerical and experimental polarization curves unreliable. We suggest characterizing the cell by first using a simplified analytical model, which contains a minimal number of parameters and ignores three-dimensional (3D) effects. The resulting physical parameters are then used as input data for a 3D numerical simulation of the PEM fuel cell. Comparison of experimental, analytical, and numerical polarization curves enables us to estimate the contribution of 3D effects to the voltage loss. This procedure is performed using specially designed experiments, our recent analytical model, and the newest version of a numerical quasi-3D model of a cell. The results show that this approach may serve as a tool for the optimization of the flow field design.
 [DOI: 10.1149/1.1914746]

Manuscript submitted July 23, 2004; revised manuscript received December 16, 2004. Available electronically May 16, 2005. This was Paper 353 presented at the San Antonio, Texas, Meeting of the Society, May 9-14, 2004.

The performance of a polymer electrolyte fuel cell (PEFC) is determined by several tens of parameters, which describe fundamental electrochemical and physical properties of the membrane electrode assembly (MEA), operational conditions, geometry of the MEA, and the structure of the flow field. Many of these parameters are strongly coupled. For instance, an increase in temperature improves the kinetics of the electrochemical reactions but decreases water content and conductivity of a polymer electrolyte membrane (PEM). The overall effect of temperature variation hence depends on the humidification conditions, which in turn depend on the geometry of the flow field. This chain of dependencies is typical for PEM fuel cells. Obviously, experimental investigations of these dependencies are time consuming and expensive, thus the use of modeling activities is desirable.

The basic features of fuel cells can be analyzed with one-dimensional 1D models that take into account transport across the cell and ignore any variations along the cell surface.[1-6] Two-dimensional (2D) models[7-22] give more detailed information, generating a map of parameters in a cross section of the MEA in one of the two planes: across-the-channel (*x*-*y* plane, Fig. 1) or along-the-channel (*x*-*z* plane, Fig. 1). In essence, either model disregards the distribution of the parameters in the other plane.

The most detailed information is provided by fully three-dimensional (F3D) models.[23-28] However, these models are very time consuming. To reduce the run times, usually just a small fragment of the fuel cell is simulated (3D element, Fig. 1), which typically covers a 10 cm distance along the channel (in Ref. 25 and 28 small cells with a meander-like flow field are simulated). The effects specific to large cells with long meander channels are beyond the scope of F3D models. Probably for efficiency, the catalyst layers in Ref. 23-27 are replaced by infinitely thin interfaces. Our results show that the distribution of the reaction rate over the catalyst layer volume can be strongly nonuniform. This nonuniformity considerably affects the cell performance and should not be ignored.

F3D models do not utilize explicitly the advantages that stem from the remarkable feature of fuel cells: the cell sandwich is essentially a two-scale system with dramatically different transport properties on the small and large scales. The channel for the feed gas supply can be up to several meters long and has a hydraulic permeability on the order of 10^{-6} cm^2. The MEA is only several hundred micrometers thick, and the permeability of the backing layer varies in the range 10^{-8} to 10^{-10} cm^2. This two-scale nature of the cell can be used to design an efficient quasi-3D (Q3D) model, as is described here.

The cell performance is depicted by voltage-current curves that summarize the voltage losses required to generate a given current. Several empirical equations for cell performance curves have been offered.[29-33] Although they provide an excellent fit to the experimental curves, these equations contain terms that physically are not fully justified.

An equation for the voltage-current curve based on an exact asymptotic solution of the transport equations across the cell was derived in Ref. 34. In Ref. 35 this equation was further extended to take into account the effect of the finite oxygen stoichiometry ratio λ (the ratio of oxygen flux supplied to the cell to the flux of oxygen required to generate the given current). The resulting expression was used to fit the experimental voltage-current curves of a cell. This procedure gave reasonable values for the basic kinetic and transport parameters of the MEA.[35]

Can the results of fitting of the experimental polarization curves serve as input parameters for a more sophisticated Q3D modeling, and what would then give the comparison of analytical, numerical, and experimental performance curves? This work aims to answer this question. Multidimensional models usually involve up to 50 parameters, which are taken from the literature. With this number of parameters, the fitting of model results to experimental data is difficult and time consuming. Generally, it is not clear which parameter should be varied to fit the experimental curve. The situation is even more complicated if a set of performance curves rather than a single curve is fitted.

In contrast, fitting with a simple analytical formula is fast and straightforward. Parameters obtained from fitting can then be used to simulate the curve with a multidimensional (Q3D or 2D) model. Both the analytical and the numerical model must be based on the same physical assumptions; in other words, the numerical model should involve a minimal number of parameters. In this work, we demonstrate that this approach enables us to characterize MEAs, to evaluate the cell design, and to estimate the contribution of 3D effects to the cell performance.

Experimental

The experiments were performed with a single PEM fuel cell with an active area of 18 cm^2 (Fig. 2). The cell is assembled with a subgasketed-style catalyst-coated membrane by Gore (Primea Series 5620 Mesga). The thickness of the proton conducting membrane between the electrodes is 35 μm, and platinum was used as the catalyst. The catalyst loadings on the anode and cathode were 0.4 and 0.6 mg cm^{-2}, respectively.

* Electrochemical Society Active Member.
[c] On leave from: Research Computing Center, Moscow State University, 119992 Moscow, Russia.
[z] E-mail: A.Kulikovsky@fz-juelich.de

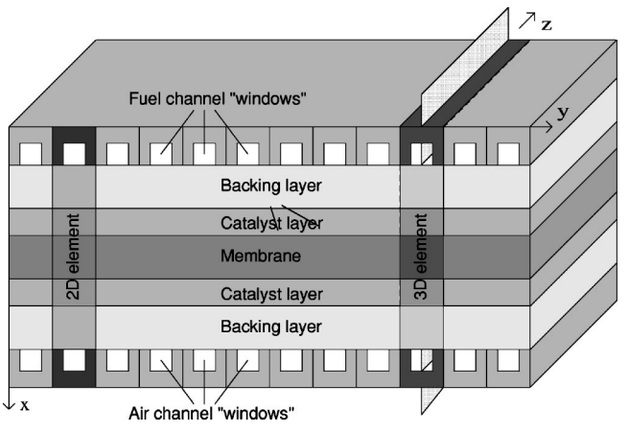

Figure 1. Sketch of the cell cross section.

Carbel CL gas-diffusion layers were placed on either side of the catalyst-coated membrane. To prevent gas leakage and to avoid excessive compression of the gas-diffusion layer, gaskets made of NBR material surrounded the diffusion layer. To ensure sufficient electrical conductivity, the diffusion layer was compressed to 40% of its original uncompressed height of 0.38 mm. The MEA was positioned between two composite-graphite current collector plates with ribbed channels for the distribution of the reactant gases. The serpentine flow configuration consists of three parallel meander channels. The channels were 1 mm deep and 1 mm wide and were separated by ribs (lands) of 1 mm width. Anode and cathode flow fields were identical.

The cell was installed between gold-coated stainless steel end plates. The cell components were held together with a set of tie rods positioned around the periphery of the cell. The tie rods were tightened with a torque wrench to ensure even distribution of the compressive force. At low current densities, the cell did not reach the desired operating temperature itself, and electrical heaters were placed behind the end plates to heat the cell. At high current densities, the cell was air cooled to maintain the operating temperature. The cell was mounted into a test rig with an electronic load. Data logging and collection were performed using a personal computer. The gas flow rate was changed with current to maintain the cell at constant stoichiometric ratios for fuel ($\lambda_{H_2} = 1.4$ and oxidant ($\lambda_{O_2} = 2$).

A point on the polarization curve was recorded when the current reached steady state, while the cell voltage was measured when it achieved a pseudo-steady state. The cell potential was taken as the potential difference between the graphite plates. Cell potential *vs.* current density measurements were made using O_2 and O_2/N_2 mixtures of different compositions. To obtain the desired cathode gas composition, pure O_2 and N_2 gas streams were controlled by two mass flow controllers; the gases were mixed before entering the cell. In all experiments pure humidified hydrogen was used as fuel. The temperature and pressure were kept constant at 70°C and 2 bars, respectively. The anode and cathode streams were humidified with deionized water by a pervaporation membrane humidifier.

Using this technique, a set of performance curves for different oxygen fractions in the cathode feed was obtained. These curves were then analyzed as described in the following sections.

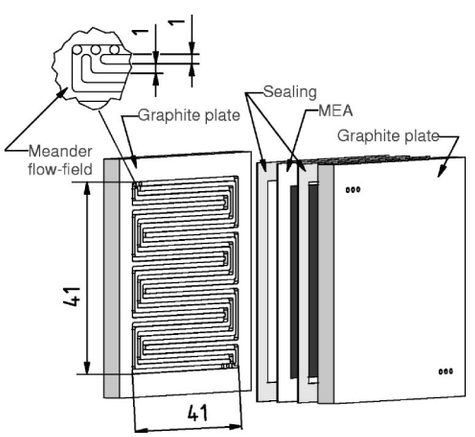

Figure 2. Sketch of the cell used in experiments. All dimensions are in millimeters.

Quasi-2D Analytical Model of a PEM Fuel Cell

Neglecting the polarization voltage on the anode side, the cell potential can be written as

$$V_{cell} = V_{oc} - \eta_c - R\bar{j} \quad [1]$$

Here V_{oc} is the open-circuit voltage, η_c is the polarization voltage of the cathode side, $\bar{j}$ is the mean current density, and $R = R_m + R_n$, where R_m is the membrane resistance and R_n accumulates the contact resistance, the resistance of the carbon phase and of the current collectors.

The cell was not disassembled during experiments; hence, R_n is constant. Furthermore, we assume that R_m (and thus R) is independent of $\bar{j}$. For thick membranes and large currents, this assumption can be violated due to the drying of the anode side of the membrane by electro-osmosis. However, if the membrane is thin and properly humidified, R_m is smaller than R_n, and to a first approximation the variation of R with $\bar{j}$ can be neglected.

The cathode polarization voltage η is given by[34-36]

$$\frac{\eta_c}{b} = \phi\left(\frac{f_\lambda \bar{j}}{j_*}\right)\ln\left(\frac{f_\lambda \bar{j}}{j_*}\right) - \ln k - \ln\left(1 - \frac{f_\lambda \bar{j}}{j_D}\right) \quad [2]$$

where the function

$$\phi(t) = 1 + \frac{t}{1+t}, \quad t = \frac{f_\lambda \bar{j}}{j_*} \quad [3]$$

varies from 1 to 2 as its argument varies from small to large values. This function matches the two exact asymptotic solutions,[34-36] obtained in the limits of $\bar{j} \ll j_*$ and $\bar{j} \gg j_*$ (small and large current densities). Here b is the Tafel slope, j_* is the characteristic current density, k accounts for the concentration overpotential, and j_D is the limiting current density due to the imperfect oxygen transport in the backing layer

$$j_* = \frac{2\sigma_t b}{l_t}, \quad k = \frac{l_t i^*}{j_*}\frac{c^0_{O_2}}{c_{O_2 ref}}, \quad j_D = 4F\frac{D_{O_2} c^0_{O_2}}{l_b} \quad [4]$$

where σ_t and l_t are the proton conductivity and the thickness of the catalyst layer, respectively, i^* is the exchange current density per unit volume, $c^0_{O_2}$ is the molar concentration of oxygen at the channel inlet, $c_{O_2 ref}$ is the reference oxygen molar concentration, and D_{O_2} is the effective diffusion coefficient of oxygen in the backing layer of the thickness l_b.

Equation 2 includes the reaction activation overpotential (the first two terms on the right side) and the voltage loss due to the imperfect oxygen transport through the backing layer (the third term on the right side). The function

$$f_\lambda = -\lambda \ln\left(1 - \frac{1}{\lambda}\right) \quad [5]$$

takes into account the effect of the stoichiometry ratio λ on the cell performance curve.[35] This function varies from infinity (as $\lambda \to 1$)

to 1 (as $\lambda \to \infty$). Equation 2 shows that the effect of finite λ is equivalent to the compression of the $\bar{j}/j_*$ coordinate by a factor of $f_\lambda \geqslant 1$. Physically, when $\lambda \gg 1$, oxygen is distributed uniformly along the channel, $f_\lambda \simeq 1$, and η does not depend on λ. However, if $\lambda \approx 1$, the oxygen concentration dramatically decreases along the channel, f_λ is large, and the limiting current density j_D appears to be f_λ times lower.

We emphasize that Eq. 2 is not an empirical relation. It follows from the exact solution of the problem of the cathode side performance.

Q3D Modeling

General description.— In this section, we describe the recent version of our Q3D model. This new version includes two-phase flow in the backing layers, the respective corrections in equations for gaseous transport, and the new boundary conditions for the problem of water transport through the membrane. Our goal is to obtain the distribution of concentrations, potentials, and currents in a cell cross section, as shown in Fig. 1. In this section, for simplicity we assume that the cell is equipped with single meander channels on both sides; the generalization to the case of several parallel meanders is obvious.

The cell cross section consists of geometrically identical 2D elements (Fig. 1). The main idea of the Q3D model is as follows. The characteristic scale of the along-the-channel variation of the local current density is much larger than the MEA thickness. This allows us to neglect the z (along-the-channel) components of currents and fluxes in the porous layers and in the membrane. The F3D problem then is split into a 2D problem in a cell cross section (internal problem) and a problem of gas flow along the channel (channel problem). Both problems are coupled by the local current density in each element.

The flow in the channel can be described by models of various complexity; the simplest is a 1D formulation. We neglect the effects due to channel curvature and consider an equivalent straight channel with the axis z directed along its axis. Consider, *e.g.*, the cathode side of the cell; oxygen in the channel is consumed in the electrochemical reaction. The continuity equation for oxygen concentration in the channel thus contains a sink term proportional to the local current density $j(z)$. For a given $j(z)$, we calculate the oxygen concentration in each "window" shown in Fig. 1. Using these concentrations as the boundary conditions, we solve the internal problem and calculate a new profile $j(z)$. (This profile is obtained by linear interpolation of the values calculated for each element.) With the new $j(z)$ we calculate new oxygen concentrations in the windows. This procedure is repeated until convergence is reached.

The advantage of this approach is that it enables effective parallelization. The internal problem is formulated for a single element, and the set of equations for each element is solved on a separate processor. Upon the completion of the iteration step, adjacent elements exchange with the "boundary conditions," as we describe here. This allows us to simulate the cells with numerous elements (*i.e.*, with technically relevant long channels).

Internal Problem

Main assumptions.—

1. The membrane is impermeable to feed gases.
2. The cell is isothermal; the fluxes due to temperature gradients are negligible.
3. Gaseous pressure on both sides of the cell is constant.
4. The flux of gases in the backing and the catalyst layers is caused by diffusion due to concentration gradients.
5. The flux of water in the membrane phase is caused by diffusion due to the concentration gradient and by electro-osmosis.
6. The membrane surface is in equilibrium with water vapor, available at the catalyst layer/membrane interface. The equilibrium is described by a water sorption isotherm.
7. The reaction rates on both sides of the cell are described by Tafel equations.
8. The dependence of capillary pressure on liquid saturation is given by the Leverett function.

Model of gas flow in porous layers.— Let the x axis be directed across the cell, the z axis is directed along the channel, and the y axis is directed parallel to the cell surface (Fig. 1). The molar flux $\mathbf{N}_i$ of the ith gas component (including water vapor) is assumed to be

$$\mathbf{N}_i = -cD_i \nabla \xi_i \qquad [6]$$

where c is the total molar concentration of the mixture, D_i is the effective diffusion coefficient (see below), and ξ_i is the molar fraction of the ith component.

We assume that Knudsen diffusion dominates in the voids of the catalyst layers and that free molecular diffusion is the main mechanism of gas transport in the backing layers. The effective diffusion coefficient D_i interpolates between the Knudsen diffusion coefficient D_i^K in the catalyst layer and the mean molecular diffusion coefficient D_i^B in the backing layer. On the anode side, the interpolation has the form

$$D_i = D_i^B + (D_i^K - D_i^B)\frac{1}{2}\left(1 - \tanh\left(\frac{x - x_0}{\Delta_0}\right)\right) \qquad [7]$$

Here x_0 is the coordinate of the backing/catalyst layer interface, Δ_0 is the thickness of the transition region, and D_i^K and D_i^B are determined by

$$D_i^K = [(1 - s)\psi]^{1.5}\bar{r}\sqrt{\frac{8RT}{\pi M_i}} \qquad [8]$$

$$\frac{[(1 - s)\varepsilon]^{1.5}}{D_i^B} = \sum_j \frac{\xi_j}{D_{ij}} \qquad [9]$$

Here s is the liquid saturation (a fraction of volume occupied by liquid water), $\bar{r}$ and ψ are the mean pore radius and the porosity of the catalyst layers, D_{ij} is the binary diffusion coefficient,[37] and ε is the porosity of the backing layers. On the cathode, side Eq. 7 has a form

$$D_i = D_i^B + \left(D_i^K - D_i^B\right)\frac{1}{2}\left(1 + \tanh\left(\frac{x - x_0}{\Delta_0}\right)\right)$$

Mass conservation of the ith component (except of water vapor, see the forthcoming discussion) reads as

$$\nabla \cdot \mathbf{N}_i = \frac{S_i}{nF} Q_{a,c} \qquad [10]$$

where $Q_{a,c}$ is the rate of the electrochemical reaction in the respective catalyst layer, S_i is the stoichiometry coefficient, and n is the number of electrons participating in the reaction. Outside the catalyst layers, $Q_a = Q_c = 0$. Substitution of Eq. 6 into Eq. 10 yields the equation for ξ_i.

Because the membrane is impermeable to gases, Eq. 10 is solved for gaseous components on both sides of the cell with a "no-flux" boundary condition at the respective membrane/catalyst layer interface. Liquid water is transported through the membrane; hence, it requires a special treatment.

Transport of liquid water.—*Flux of liquid water in the backing and catalyst layers*.—The flux of liquid water in the voids of the catalyst and backing layers is given by

$$\mathbf{N}_\ell = s\varepsilon\rho_\ell \mathbf{v}_\ell \qquad [11]$$

where s is the liquid saturation, and ρ_ℓ and $\mathbf{v}_\ell$ are the density and velocity of liquid water. Assuming Poiseuille flow in the pores, $\mathbf{v}_\ell$ is proportional to the liquid pressure gradient:

$$\mathbf{v}_\ell = -\frac{k_p}{\mu_\ell} \nabla p_\ell \quad [12]$$

where k_p is the hydraulic permeability of the porous media and μ_l is the viscosity of liquid water. We assume that the permeabilities of the backing and catalyst layer coincide.

The liquid pressure is $p_\ell = p_g - p_c$, where p_g and p_c are the gaseous and capillary pressures, respectively. Neglecting the gradient of gaseous pressure, we write

$$\mathbf{v}_\ell = \frac{k_p}{\mu_\ell}\nabla p_c = \frac{k_p}{\mu_\ell}\frac{\partial p_c}{\partial s}\nabla s = s\frac{k_p^0}{\mu_\ell}\frac{\partial p_c}{\partial s}\nabla s \quad [13]$$

Here k_p^0 is the hydraulic permeability of a dry backing layer. Following Ref. 18 and 19 we have assumed that $k_p^l = sk_p^0$.

Following Leverett,[38] the capillary pressure is given by

$$p_c = \sigma\sqrt{\frac{\varepsilon}{k_p^0}}f(s) \quad [14]$$

where σ is the surface tension and $f(s)$ is the empirical function[39]

$$f(s) = 1.417(1-s) - 2.120(1-s)^2 + 1.263(1-s)^3 \quad [15]$$

Collecting everything we get[27]

$$\mathbf{N}_\ell = -\rho_l D_s \nabla s \quad [16]$$

where

$$D_s = -\left(\frac{s^2\sigma\varepsilon\sqrt{\varepsilon k_p^0}}{\mu_\ell}\right)\frac{\partial f}{\partial s} \quad [17]$$

Note that $D_s > 0$ because $\partial f/\partial s < 0$.

Water in the membrane and in the catalyst layers.— In this subsection, we describe the modification of the model[40,41] due to the two-phase nature of water flow in the backing and catalyst layers. We assume that the transport of liquid water in the membrane is caused by diffusion due to a concentration gradient and by electro-osmosis. Thus, the flux of liquid water in the membrane $\mathbf{N}_\ell$ is

$$\mathbf{N}_\ell = -D_\ell(\zeta)\nabla c_\ell + n_d(\zeta)\frac{\mathbf{j}_m}{F} \quad [18]$$

where ζ is the membrane water content (the number of water molecules per SO_3^- group), c_l and D_l are the concentration and diffusion coefficients of liquid water, respectively, and $n_d(\zeta)$ is the drag coefficient.

Three mechanisms contribute to water transport in the catalyst layers: diffusion and drag of liquid water in the membrane phase and Knudsen diffusion of vapor in the voids. The flux of water in the membrane phase is given by Eq. 18, multiplied by a correction factor ε_m, the volume fraction of electrolyte in the active layer. The total flux of water in the catalyst layer then is

$$\mathbf{N}_w = -D_w^K c\nabla\xi_w + \varepsilon_m\left(-D_\ell(\zeta)\nabla c_\ell + n_d(\zeta)\frac{\mathbf{j}_m}{F}\right) \quad [19]$$

where ξ_w is the molar fraction of vapor and D_w^K is given by Eq. 8.

We assume that the local concentration of liquid water in the membrane phase is related to the local concentration of vapor via a sorption isotherm $\Lambda(a)$[42]

$$\zeta \equiv \frac{c_\ell}{c_{H^+}} = \Lambda(a) = \Lambda\left(\frac{c_w}{c_w^{sat}}\right) \quad [20]$$

where $a \equiv c_w/c_w^{sat}$ is the water activity and c_w^{sat} is the molar concentration of saturated vapor. With Eq. 20 we can write the diffusion component of the liquid water flux as

$$-D_\ell\nabla c_\ell = -D_\ell\frac{c_{H^+}}{c_w^{sat}}\left(\frac{\partial\Lambda}{\partial a}\right)c\nabla\xi_w = -D_w c\nabla\xi_w \quad [21]$$

where

$$D_w = D_\ell\frac{c_{H^+}}{c_w^{sat}}\left(\frac{\partial\Lambda}{\partial a}\right) \quad [22]$$

is the diffusion coefficient of equivalent water vapor. Finally, in the catalyst layers we have

$$\mathbf{N}_w = -D_w^K\nabla c_w + \varepsilon_m\left(-D_w(\zeta)\nabla c_w + n_d(\zeta)\frac{\mathbf{j}_m}{F}\right) \quad [23]$$

Mass balance of water.— Mass conservation means that $\nabla\cdot\mathbf{N} = R$, where R is the respective rate of species production/consumption. With the flux equation (Eq. 16), we get the diffusion equation for saturation

$$-\nabla\cdot(D_s\nabla s) = \frac{M_w}{\rho_\ell}(R_\ell^{ORR} + R_\ell^{ec}) \quad [24]$$

where M_w is the molecular weight of water, R_ℓ^{ORR} is the molar rate (mol cm^{-3} s^{-1}) of liquid water production in an oxygen reduction reaction (ORR) and R_ℓ^{ec} is the molar rate of liquid water consumption/production due to evaporation/condensation.

For R_ℓ^{ORR} we have $R_\ell^{ORR} = S_w Q_c/nF$, where Q_c is the rate of ORR (a number of protons consumed in unit volume per second, see later discussion). R_ℓ^{ec} is given by He *et al.*[18]

$$R_\ell^{ec} = -\varepsilon s K_e(c_w^{sat} - c_w)r - \varepsilon(1-s)K_c\xi_w(c_w^{sat} - c_w)(1-r) \quad [25]$$

where the first and second terms describe the rate of evaporation and condensation, respectively (K_e and K_c are evaporation and condensation frequencies, s^{-1}), and the function

$$r = \frac{1}{2}\left(1 + \frac{|c_w^{sat} - c_w|}{c_w^{sat} - c_w}\right) \quad [26]$$

switches in the Eq. 25 evaporation or condensation term depending on the sign of $c_w^{sat} - c_w$. The mass conservation equation for water vapor has the form

$$\nabla\cdot\mathbf{N}_w = -R_l^{ec} \quad [27]$$

where $\mathbf{N}_w$ is given by Eq. 6 and 23 in the backing and catalyst layers, respectively.

Water content of membrane phase.— Due to the presence of liquid water, the local water content of the membrane phase in the catalyst layer increases. To describe the effect of the coexistence of liquid- and gas-phase water, we introduce the effective water content of the membrane phase ζ_{eff}

$$\zeta_{eff} = (1-s)\zeta + s\zeta_{max} \quad [28]$$

where $\zeta = \Lambda(c_w/c_w^{sat})$ and $\zeta_{max} = 22$ is the water content of the membrane phase in contact with liquid water. Equation 28 is also used to calculate the water content of the surface of the bulk membrane, which gives boundary conditions for the problem of water transport in the membrane.

Potentials and reaction rates.— Physically, the electrochemical reactions occur in a high electric field of a double layer created at the metal/electrolyte interfaces. In the porous catalyst layers, the double layers form complex tortuous structures. In the fuel cell modeling the distribution of the electric field in these structures is simulated by a continuous distribution of two potentials: $\varphi_{a,c}$, the potential of carbon threads interconnecting catalyst particles, and φ_m, the potential of the polymer electrolyte phase, which provides the transport of protons to the catalyst sites. The difference between these potentials determines the rate of the electrochemical reaction.

The potentials φ_m and $\varphi_{a,c}$ are governed by the proton and electron current conservation equations

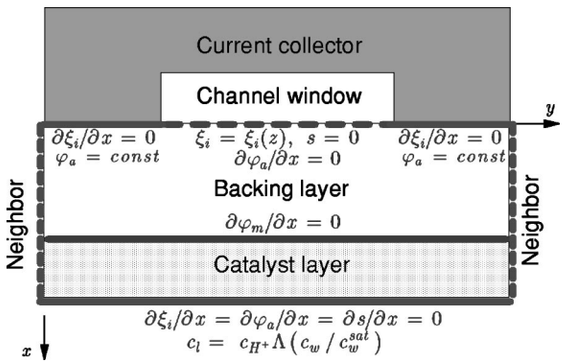

Figure 3. Boundary conditions for anode side of a single 2D element (see Fig. 1). Boundary conditions for cathode side are analogous.

$$\nabla \cdot (\sigma_m(\zeta)\varphi_m) = \begin{cases} -Q_a & \text{in the anode catalyst layer} \\ Q_c & \text{in the cathode catalyst layer} \\ 0 & \text{otherwise} \end{cases} \quad [29]$$

$$\nabla \cdot (\sigma_a\varphi_a) = \begin{cases} Q_a & \text{in the anode catalyst layer} \\ 0 & \text{otherwise} \end{cases} \quad [30]$$

$$\nabla \cdot (\sigma_c\varphi_c) = \begin{cases} -Q_c & \text{in the cathode catalyst layer} \\ 0 & \text{otherwise} \end{cases} \quad [31]$$

where σ_m is the conductivity of the membrane phase and σ_a,σ_c are the conductivities of the carbon phases at the anode and the cathode side, respectively. In the catalyst layers, $\sigma_m(\zeta) = \varepsilon_m\sigma_m^{bulk}(\zeta)$, where σ_m^{bulk} is the proton conductivity of the bulk membrane. The dependence $\sigma_m^{bulk}(\zeta)$ is linear (see Ref. 41 for details).

For comparison with the analytical theory, in this work, the rates of hydrogen oxidation and oxygen reduction reactions are described by Tafel equations

$$Q_a = i_a^* \frac{c_{H_2}}{c_{H_2 ref}} \exp\left(\frac{\alpha_a F}{RT}\eta_a\right) \quad [32]$$

$$Q_c = i_c^* \frac{c_{O_2}}{c_{O_2 ref}} \exp\left(\frac{\alpha_c F}{RT}\eta_c\right) \quad [33]$$

Here Q is the number of protons produced/consumed per unit volume per unit time, i^* is the exchange current density (per unit volume), c_{ref} is the reference molar concentration of the feed gas, α is the transfer coefficient, and the subscripts a and c refer to the anode and the cathode side, respectively. The overpotentials $\eta_a = \varphi_a - \varphi_m$ and $\eta_c = \varphi_m - \varphi_c$ are positive. Because the voltage loss due to anodic reaction is negligible, the contribution of reaction terms to the cell performance is governed by just two parameters: $i_c^*/c_{O_2 ref}$ and α_c. Applying a more sophisticated reaction scheme would only complicate the analysis of the results.

Boundary conditions.— Boundary conditions for the anode side of a single element are shown in Fig. 3. At the current collector/backing layer interface, the carbon phase potential is fixed and the normal component of all fluxes is zero. At the channel/backing layer interface, the molar fraction of gases and the concentration of water vapor are obtained from the channel problem. Liquid saturation along this interface is assumed to be zero due to rapid removal of liquid water by the flow in the channel. Along the backing layer/catalyst layer interface, the normal component of proton current is zero. Along the catalyst layer/membrane interface, the normal components of all fluxes (except that of liquid water) are zero. According to our assumptions, the hydrodynamic mechanism of liquid water transport changes from D'Arcy flow (viscous convection) in the catalyst layer to diffusion due to the concentration gradient in the bulk membrane; we thus put $\partial s/\partial x = 0$ at the catalyst layer/membrane interface.

The mass balance equations for water are solved separately, first in the backing and catalyst layers and then in the membrane. At the catalyst layer/membrane interface Eq. 20 relates the concentration of liquid water in the membrane to the concentration of water vapor in the catalyst layer.

Channel problem.— Laminar steady flow in a long channel with impermeable walls is basically the Poiseuille flow with constant velocity determined by the pressure gradient. However, due to electrochemical reactions, the velocity in the fuel cell channel may vary with the distance z. A 1D model of the gas flow in the fuel cell channel[43] shows that the flow is incompressible: $\rho(z) \simeq \rho^0$, where ρ^0 is the flow density at the inlet. The velocity distribution then is obtained from the mass balance equation. In the cathode channel, this equation reads as

$$\rho^0 \frac{\partial v}{\partial z} = \frac{[2(1+2a)M_w - M_{O_2}]\, j(z)}{4Fh} \quad [34]$$

where v is the flow velocity, h is the channel height, M is the molecular weight, and a is the effective coefficient of water transport through the membrane. The latter is defined as the number of water molecules transported from the anode to the cathode per each proton. Note that a coincides with the drag coefficient n^d only when the back-diffusion flux of water in the membrane is negligible. The solution to Eq. 34 gives $v(z)$; the oxygen mass balance

$$\frac{\partial(v c_{O_2})}{\partial z} = -\frac{j(z)}{4Fh} \quad [35]$$

then gives the profile of the oxygen molar concentration $c_{O_2}(z)$. Similar equations are written for hydrogen in the anode channel.

Numerical aspects.— The conservation equations lead to convection-diffusion equations of the type

$$\nabla \cdot (-D\nabla u + \mathbf{W}u) = q \quad [36]$$

where D is the diffusion coefficient and $\mathbf{W}$ is the "convective" velocity. The concentrations of gaseous components in the backing and catalyst layers are given by Eq. 36 with $W = 0$ and $D = D(\mathbf{r})$, a function of the coordinates. Water transport in the membrane is governed by a nonlinear version of Eq. 36 with $\mathbf{W} \neq 0$ and $D = D(u)$. Equations 29-31 formally have the form of Eq. 36 with $W = 0$ and $D = \text{const}$.

An internal model is formulated for a single 2D element (Fig. 1). We introduce a nonuniform rectangular grid, which covers the element (Fig. 4). Equation 36 is converted to the finite difference form with the method of control volume. If $D = D(\mathbf{r})$, the fluxes through the surfaces of the computational cell are calculated with the Scharfetter-Gummel scheme.[44] In the nonlinear case, $D = D(u)$ and the fluxes are calculated with the q-scheme.[45] Equations for the potentials in Eq. 29-31 are approximated on a five-point computational molecule, as described in Ref. 10. Equation 29 is subject to Neumann boundary conditions $\partial\varphi_m/\partial x = 0$ along the backing/catalyst layer interfaces (Fig. 3). The unique solution is selected by the condition that the reactions on both sides of the cell produce/consume the same current (see Ref. 11 for details).

To accelerate convergence, Newton's method is employed for each equation. In all cases, the resulting system of linear algebraic equations is solved with the standard iteration technique SOR. Typically, the computational grid for a single element has 100×200 nodes along the x and y axes, respectively.

Let the along-the-channel profile of the current density $j(z)$ be known. (Along both channels these profiles are the same.) The full iteration step consists of the following substeps.

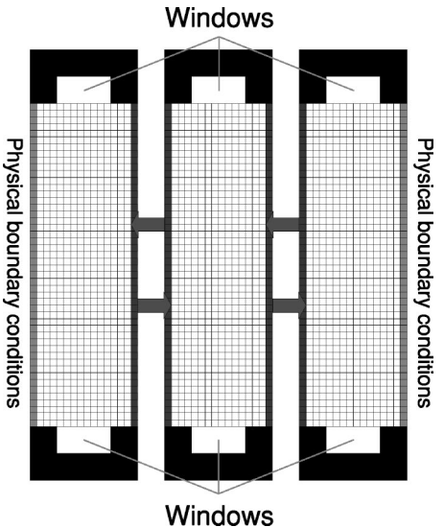

Figure 4. Illustration of the idea of parallel algorithm.

1. For a given $j(z)$, the channel problem is solved for both the anode and the cathode channels; this gives the gas concentrations in all "windows" (Fig. 1).
2. For all 2D elements (Fig. 1), the internal problem is solved using as the boundary conditions the concentrations obtained in step 1.
3. "Boundary conditions" between adjacent elements are exchanged (Fig. 4).
4. A new $j(z)$ is calculated.

A typical calculation of the polarization curve requires about 10 h on a cluster of PCs based on 2 GHz processors.

Results

Analytical model.—To take into account the effect of a finite oxygen stoichiometry λ on the cell performance, the experimental data were corrected according to Eq. 2. For each experimental point $(\bar{j}, V_{\text{cell}})$, the values of j were multiplied by $f_\lambda = 1.386$, which corresponds to $\lambda = 2.0$. This somewhat overestimates the cell performance as the model[35] does not take into account the effect of nonuniformity of water concentration along the channel. Nevertheless, λ-corrected curves lead to a more realistic set of fitting parameters.

Equations 1 and 2 were then used to fit the experimental voltage current curves. These equations contain five fitting parameters: b, j_*, k, j_D, and R. The fitting procedure is based on a genetic algorithm.[46] The results of the fitting are shown in Fig. 5. The accuracy of the fitting turned out to be high; the correlation coefficient for all curves exceeds 0.99. The fitting parameters are listed in Table I. Physically, three of these parameters should not depend on the oxygen concentration; the respective mean values are shown in the last column of Table I.

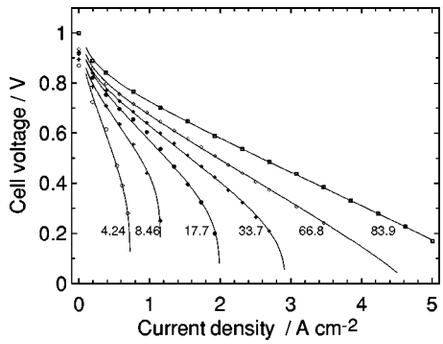

Figure 5. Experimental points and fitting curves (Eq. 1 and 2) for indicated values of oxygen concentration (%) in N_2-O_2 mixture. Experimental conditions are listed in Table III. The experimental data are λ-corrected (see text).

The Tafel slopes for all curves exhibit only minor differences, with an average of 57 mV (131 mV/dec). At a temperature of 70°C, this is equivalent to the effective transfer coefficient $\alpha = RT/(bF) = 0.518$. The characteristic current density j_* varies in the range 2.5-4.6 A cm^{-2} with the average value 3.62 A cm^{-2}. For oxygen concentrations above 9%, j_* is comparable to the limiting current density j_D (Table I). Therefore, under medium and high oxygen content, the cell operates in the intermediate regime ($\bar{j} \simeq j_*$), and the apparent Tafel slope $b_{\text{app}} = \varphi b$ significantly exceeds b (Eq. 2). b_{app} estimated as $b_{\text{app}} \approx b\varphi(j_D/j_*)$ is shown in the second row of Table I. For all oxygen contents, j_* and b are nearly constant (Table I). The ratio j_D/j_* then increases with the growth of inlet oxygen concentration $c^0_{O_2}$ due to the increase in j_D. Therefore, b_{app} increases with $c^0_{O_2}$ because the function φ increases. Physically, with the growth of the oxygen fraction, the regime of the catalyst layer operation is going from the low-current to the high-current one. In the high-current regime, the rate of ORR is strongly nonuniform across the catalyst layer, b_{app} is twice larger than in the low-current regime, and the cell performance dramatically degrades. To keep the cell in the low-current regime ($\bar{j} \ll j_*$), the value of j_* must be increased. Because $j_* \approx \sigma_m/l_t$, it is beneficial to increase the conductivity of the membrane phase in the catalyst layer or to decrease the layer thickness l_t.

As predicted by Eq. 4, the limiting current density j_D is proportional to the oxygen concentration (Fig. 6). The slope of the straight line in Fig. 6 determines the effective diffusion coefficient of oxygen in the backing layer $D^{\text{Q2D}}_{O_2} = 5.32 \times 10^{-3}$ cm^2 s^{-1}, where the superscript Q2D indicates that the value is obtained from the analytical Q2D model. The effective oxygen diffusion coefficient in the backing layer, calculated from Eq. 9 with $\varepsilon = 0.4$ and $s = 0$, amounts to $D^{\text{B,dry}}_{O_2} = 4.8 \times 10^{-2}$ cm^2 s^{-1}. The value resulting from the fitting is thus about 10 times lower. Later we show that this discrepancy can serve as a measure of voltage loss due to 3D effects in oxygen distribution.

Table I. Fitting parameters: b Tafel slope, b_{app} apparent Tafel slope, j_* characteristic current density, j_D limiting current density, and R cell resistance (the sum of the membrane and contact resistance).

O_2 fraction (%)	4.24	8.46	17.7	33.7	66.8	83.9	Mean
b (mV)	55.4	57.4	57.5	55.4	59.2	57.2	57.0
b_{app} (mV)	65.7	69.3	79.5	85.1	93.8	92.0	-
j_* (A cm^{-2})	3.18	4.45	3.23	2.55	3.66	4.65	3.62
j_D (A cm^{-2})	0.727	1.16	2.00	2.94	5.15	7.24	-
$-\ln(k)$	9.58	9.84	9.84	9.14	8.83	8.78	-
R (mΩ cm^2)	503	224	224	138	116	96	211

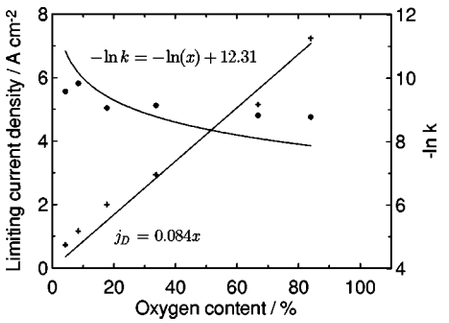

Figure 6. Limiting current density j_D (crosses) and the term $-\ln k$ in Eq. 2 (filled circles) as a function of oxygen concentration. Solid lines: linear fit for j_D and logarithmic fit (Eq. 37) for $-\ln k$. The quality of fitting of $-\ln k$ is poor; the respective fitting parameters give just a rough estimate of exchange current density.

The value $-\ln k$ exhibits the proper trend: it decreases with the growth of oxygen content (Fig. 6). The dependence of $-\ln k$ on c_{O_2} was fit with Eq. 4 for k

$$y = -\ln k = -\ln\left(100\frac{c^0_{O_2}}{c}\right) - \ln\left(\frac{l_t i^*}{j_* 100\dfrac{c_{O_2 ref}}{c}}\right) \qquad [37]$$

where c is the total molar concentration of the gas mixture.

Fitting the points in Fig. 6, we get the value of the second term on the right side of Eq. 37, which appears to be 12.31. Equation 4 then enables us to estimate the ratio $i^*/c_{O_{2ref}}$, which amounts to $i^*/c_{O_{2ref}} = 2.2 \times 10^4$ A mol^{-1}. (See Table II.) The quality of the fitting of $-\ln k$ is rather poor, so this value is only a rough estimate.

The cell resistivity R (Table I) decreases with increasing oxygen content. We attribute this to the effects of water management, which are not taken into account in the analytical model. However, the mean value of R resulting from the fitting (211 mΩ cm^2) is close to the measured one (180 mΩ cm^2).

Q3D results.—The parameters resulting from the fitting (Table II) were used as input data for the Q3D simulation. Because of the great practical importance, the case of 17.7% oxygen content (humidified air) was simulated. The operating conditions and the other required parameters are listed in Table III. For comparison with the analytical theory, we set $D^K_{O_2} = D^B_{O_2}$, *i.e.*, the oxygen transport in the catalyst and backing layers was described by the same effective diffusion coefficient.

Figure 7 shows the experimental, analytical, and simulated voltage-current curves. Note that for proper comparison all curves in Fig. 7 are "lambda corrected" (*i.e.*, according to Eq. 5, the current density is multiplied by 1.386, which corresponds to $\lambda = 2$). Furthermore, because the Q3D model does not take into account the contact resistance, the resulting polarization curves are further corrected according to $V^{IR}_{cell} = V_{cell} - j(0.180 - R_m)$, where R_m is the calculated value of the resistance of the membrane and the catalyst layers, and 0.180 Ω cm^2 is the measured total cell resistance. The result is the thick solid curve (Fig. 7). The limiting current density resulting from the Q3D simulation is significantly lower than the experimental value (Fig. 7). The reason is a strong nonuniformity of oxygen distribution over the catalyst layer volume, as discussed here.

Table II. Transport and kinetic parameters resulting from the fitting.

Parameter	Value
α	0.518
$i^*/c_{O_{2ref}}$ (A mol^{-1})	2.2×10^4
D_{O_2} (cm^2 s^{-1})	5.32×10^{-3}

Table III. Conditions and parameters for Q3D simulation.

	Anode side	Cathode side
Cell temperature (°C)	70	70
Inlet parameters:		
Gas pressure (atm)	2	2
Flow stoichiometry	1.4	2.0
Oxygen molar fraction	-	0.177
Nitrogen molar fraction	-	0.667
Water vapor molar fraction	0.168	0.156
Hydrogen molar fraction	0.832	-
Volume fraction of electrolyte in catalyst layers ε_m	0.1	0.1
Porosity of backing layers ε	0.4	0.4
Porosity of catalyst layers ψ	0.2	0.2
Mean pore radius $\bar{r}$ in Eq. 7 (cm)	10^{-6}	10^{-6}
Frequency of evaporation/ condensation		
$K_e = K_c$ (s^{-1})	10^2	
Carbon phase conductivity (Ω^{-1} cm^{-1})	40	
Catalyst layer thickness (μm)	10	
Backing layer thickness (μm)	150	
Membrane thickness (μm)	35	
Channel width (cm)	0.1	
Channel height (cm)	0.1	
Current collector width (cm)	0.1	

With a six times higher oxygen diffusion coefficient $D^{Q3D}_{O_2} = 3.2 \times 10^{-2}$ cm^2 s^{-1}, the Q3D model generates the dashed curve in Fig. 7. Unfortunately, we were not able to extend this curve to larger values of $\bar{j}$. At $f_\lambda \bar{j} \simeq 1275$ mA cm^{-2}, a loss of convergence occurs due to a very low water concentration in front of the current collector ribs on the anode side (see Fig. 9 later). Nevertheless, in the range $f_\lambda \bar{j} \leqslant 1275$ mA cm^{-2}, the dashed curve is in good agreement with the experimental data.

Figure 8 shows the detailed maps of parameters in the MEA cross section for two current densities ($f_\lambda \bar{j} = 346$ and 1275 mA cm^{-2}). In both cases, the rate of ORR Q_c follows the pattern of oxygen concentration in the catalyst layer. When the current density is small (Fig. 8, left), the nonuniformity of the parameters distribution over the catalyst layer volume is not large. The

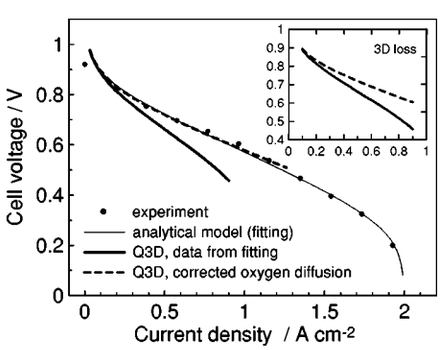

Figure 7. Voltage-current curves for 17.7% oxygen concentration (synthetic air). Dots: experiment; thin solid line: fit with Eq. 1 and 2; thick solid curve: result of Q3D simulation with parameters resulted from fitting; dashed curve: Q3D simulation with 6 times larger oxygen diffusion coefficient. Inset: Difference between two curves resulting from Q3D (dotted area) shows contribution of 3D effects in oxygen transport to the voltage loss.

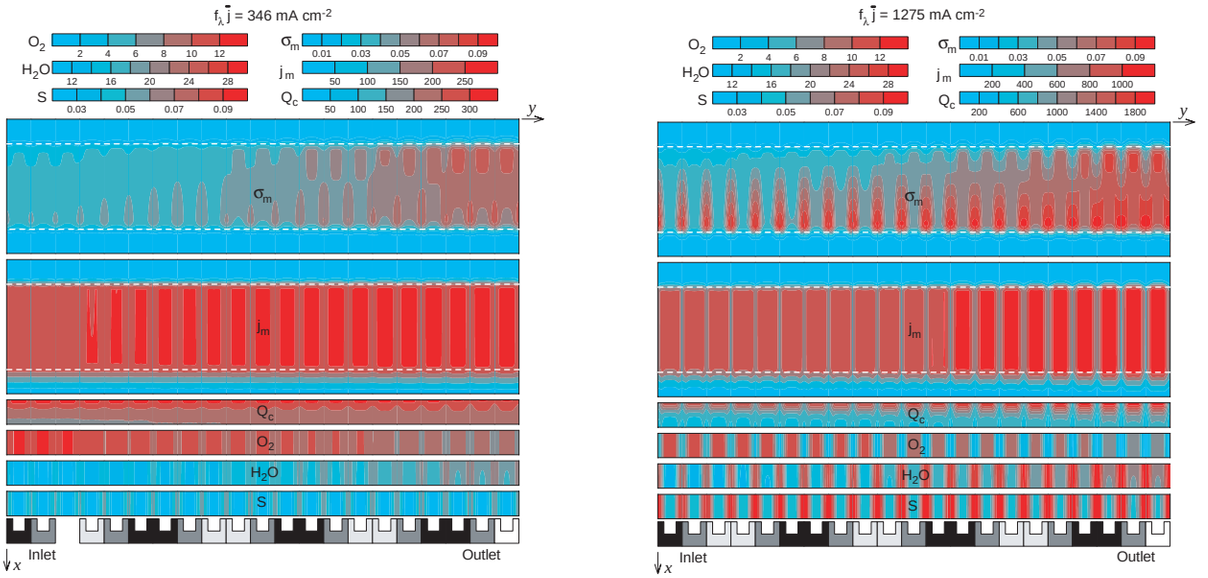

Figure 8. 3D maps of parameters for mean current densities: (left) $f_\lambda \bar{j}$ = 346 mA cm^{-2} and (right) 1275 mA cm^{-2}. Shown are (from top to bottom) proton conductivity of membrane phase σ_m (Ω^{-1} cm^{-1}), proton current density in membrane and in catalyst layers j_m (mA cm^{-2}), rate of electrochemical reaction Q_c (A cm^{-3}), oxygen and water molar concentrations (10^{-6} mol cm^{-3}) in cathode catalyst layer, and liquid saturation s. White dashed line indicates the catalyst layer/membrane interfaces.

variation of Q_c across the active layer is also small (Fig. 8, left), indicating that the layer operates in the low-current regime. Under high current density ($f_\lambda j$ = 1275 mA cm^{-2}, Fig. 8, right) the mode of the catalyst layer operation dramatically changes. The distribution of the reaction rate, both across and along the catalyst layer, appears to be strongly nonuniform. Most of the proton current is converted in front of the feed channel in a thin sublayer, close to the membrane surface (Fig. 8, right). A detailed map of the parameters in the first two elements at the inlet is shown in Fig. 9. Due to the lack of oxygen in front of the current collector ribs, the reaction rate there is low and almost uniform across the layer (Fig. 9). These domains hence operate in a low-current regime. However, in front of the channel, the profile $Q_c(x)$ is strongly nonuniform, indicating that this domain operates in the high-current regime. Figure 9 demonstrates the interesting effect of coexistence of the high- and low-current regimes in the adjacent domains of the active layer.

The local nonuniformity of oxygen concentration in each element (Fig. 8, right) explains the difference between the diffusion coefficients resulting from the analytical theory and from the Q3D model. The analytical model ignores these local features of the oxygen distribution; this model thus tends to underestimate the oxygen diffusion coefficient. The analytical model replaces the 2D flow with the equivalent 1D flow, which gives the same voltage loss. The difference between the two curves resulting from Q3D modeling (Fig. 7) may thus serve as an estimate of the voltage loss due to 3D effects in the oxygen transport (inset in Fig. 7). The good agreement of the experimental, analytical, and numerical curves in Fig. 7 substantiates that Fig. 8 is likely to give a correct qualitative picture of the cell operation. This figure shows that for this particular cell design the main problems are formation of oxygen-depleted zones in front of the current collector ribs and "contraction" of the reaction rate in a thin sublayer close to the membrane surface.

The value $D_{O_2}^{Q3D} = 3.2 \times 10^{-2}$ cm^2 s^{-1}, which provides agreement of simulated and experimental polarization curves, is close to the binary diffusion coefficient of oxygen in the dry backing layer $D_{O_2}^{B,dry}$ (4.8×10^{-2} cm^2 s^{-1}, Eq. 9). In our calculations, the liquid saturation does not exceed 10% (Fig. 8, right); thus, the decrease in oxygen diffusivity due to partial flooding of the backing layer is small.

Discussion

The analytical model is based on the assumption that, on average, oxygen transport can be described by a constant position-independent diffusion coefficient. Then, according to Eq. 4, the limiting current density j_D must be proportional to c_{O_2}. The linear dependence in Fig. 6 is a strong argument in favor of this assumption. This allows us to roughly characterize transport properties of the cathode side by a single parameter: the effective diffusion coefficient $D_{O_2}^{Q2D}$. The polarization curves resulting from the Q3D simulations do not follow the linear trend $j_D \sim c_{O_2}$: the limiting current densities for the thick curves in Fig. 7 differ by a factor of 2, whereas the respective oxygen diffusion coefficients differ by a factor of 6. This is not surprising, as the through-plane transport of oxygen is strongly influenced by local 2D effects due to channel/rib alternation (Fig. 8). The analytical model replaces the 2D flow with the equivalent 1D flow; it appears that the integral parameter $D_{O_2}^{1D}$ provides a linear relation $j_D \sim c_{O_2}$. This parameter is thus suitable for cell characterization.

The analytical model ignores the transport of oxygen in the catalyst layer. In some situations (*e.g.*, when the catalyst layer is very thick or if it has very low porosity), this model is inapplicable due to the strong variation of oxygen concentration across the active layer.

The variation of cell resistance with oxygen content (Table I) indicates that under high current density membrane drying comes into play, and the analytical model should be modified to take into account the effects of water management.[47,48] This work is in progress.

The models[14,27] give low values of liquid saturation in a cell. The model[18,19] gives, in contrast, almost 100% saturation under high currents. In Ref. 27 this difference is attributed to a 4 orders of magnitude higher liquid water diffusivity than that in Ref. 18 and 19

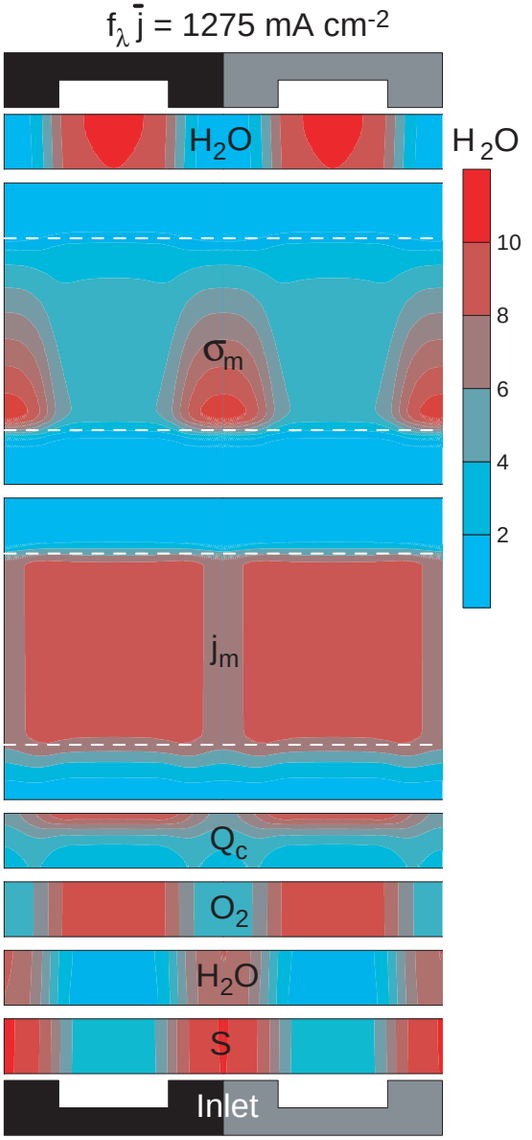

Figure 9. Detailed map of parameters in first two elements at inlet for a mean current density of $f_{el}\bar{j}$ = 1275 mA cm^{-2} (cf. Fig. 8, right). Color scales and designations are same as in Fig. 8, right. Concentration of water vapor in anode catalyst layer is also shown (10^{-6} mol cm^{-3}).

(see the Appendix for a detailed explanation). Maximal saturation in our model is regulated by the frequencies of condensation K_c and evaporation K_e in Eq. 25 (see the Appendix). For real backing layers, K_c and K_e are poorly known; the values used here (Table III) are chosen to provide 10% maximal saturation (Fig. 8, right). The question of what the average liquid saturation in a cell is and how this value depends on the properties of the backing layer remains open.

The preceding results suggest the following strategy of cell optimization. First, the cell is described by a minimal set of five parameters: $D_{O_2}^{1D}$, α, $i^*/c_{O_2 ref}$, j_*, and R. Estimates of these parameters are obtained from the fitting of the experimental voltage-current curves with the analytical formulas (Eq. 1 and 2). Note that more reliable results are obtained if a set of curves rather than a single curve is fitted.

The physical parameters resulted from the fitting are then used to simulate the cell with the more sophisticated (Q3D) numerical model, which takes into account 3D effects. Comparison of the analytical and simulated curves enables us to estimate the contribution of 3D effects to voltage loss.

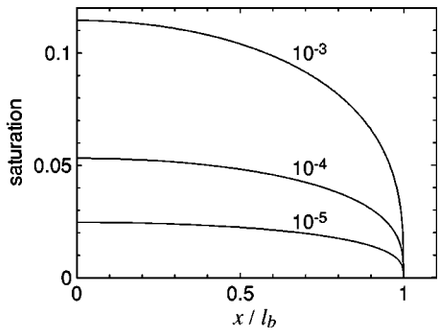

Figure A-1. Liquid saturation s (Eq. A-5) in cathode backing layer for indicated values of parameter γ. Membrane is at $x/l_b = 0$; backing layer/channel interface is at $x/l_b = 1$.

The maps in Fig. 8 provide a qualitative picture of the physical processes occurring inside the cell. Under high current density, the contraction of the reaction rate close to the surface of the membrane and the formation of oxygen-depleted zones are clearly seen. Generally, these phenomena reduce the cell performance. For its computational efficiency, the optimization tool described above is suitable for parameter variation in the practical fuel cell development. The optimization goals for the cell used in this work are to eliminate the shaded zones and to optimize the thickness of the active layer.

Conclusions

We suggest a novel approach to the analysis of experimental performance curves of a PEM fuel cell. The idea is to use a hierarchy of models for analysis rather than a single model. In the simplest case, this hierarchy consists of just two models: low-level analytical and high-level numerical. The analytical model serves for a fast estimate of the basic transport and kinetic parameters of the cell. The resulting parameters are then used as input data for a more accurate numerical model. Comparison of the experimental, analytical, and numerical polarization curves enables us to estimate the contribution of the effects, which are beyond the scope of a low-level model.

This procedure is performed using our recent quasi-2D analytical (low level) and the newest version of numerical Q3D (high-level) models of a cell. The analytical model accounts for the transport of oxygen across the cell and along the feed channel and ignores local 2D effects in the through-plane oxygen transport. The two-phase, Q3D numerical model takes into account all the basic processes in the cell. Comparison of the analytical and numerical polarization curves enables us to evaluate the contribution of local 2D effects in oxygen transport to the overall voltage loss. This procedure may serve as a tool for optimization of the flow field design.

The Institute for Materials and Processes in Energy Systems assisted in meeting the publication costs of this article.

Appendix

Analytical Solution of Equation for Liquid Saturation

To understand the character of the solution to Eq. 24, consider the following simple model. We assume that ORR generates water vapor, *i.e.*, in Eq. 24, $R_l^{ORR} = 0$. If the cell temperature is not high, liquid saturation is due to the condensation. We have $c_w^{sat} < c_w$, $r = 0$, and the first term on the right side of Eq. 25 is zero. The 1D-variant of Eq. 24 along x (Fig. A-1) then takes the form

$$\frac{\partial}{\partial x}\left(D_s \frac{\partial s}{\partial x}\right) = \frac{M_w}{\rho_l}\varepsilon(1-s)K_c\xi_w(c_w^{sat} - c_w) \qquad [A\text{-}1]$$

or

$$-\frac{\partial}{\partial\tilde{x}}\left(s^2\frac{\partial f}{\partial s}\frac{\partial s}{\partial\tilde{x}}\right) = \gamma(1-s) \qquad [A\text{-}2]$$

Here

$$\gamma = \frac{M_w\mu_l K_c\xi_w(c_w - c_w^{sat})l_b^2}{\rho_l\sigma\sqrt{\varepsilon k_p^0}} \qquad [A\text{-}3]$$

l_b is the thickness of the backing layer, and the dimensionless coordinate $\tilde{x} = x/l_b$ ($\tilde{x} = 0$ is at the cathode side of the membrane, $\tilde{x} = 1$ is at the cathode backing layer/channel interface).

We assume that the saturation is small: $s \ll 1$. This assumption only limits the range of variation of parameter γ. For small s we may put $1 - s \simeq 1$ and $\partial f/\partial s \simeq -1$ (this is evident if one calculates $\partial f/\partial s$ for small s from Eq. 15). Equation A-2 then reduces to

$$-\frac{\partial}{\partial\tilde{x}}\left(s^2\frac{\partial s}{\partial\tilde{x}}\right) = \gamma, \qquad \left.\frac{\partial s}{\partial\tilde{x}}\right|_{\tilde{x}=0} = 0, \qquad s|_{\tilde{x}=1} = 0 \qquad [A\text{-}4]$$

The boundary conditions are discussed in the section on boundary conditions.

The solution to the problem A-4 is

$$s = \left(\frac{3\gamma(1-\tilde{x}^2)}{2}\right)^{1/3} \qquad [A\text{-}5]$$

This solution is shown in Fig. A-1 for several values of parameter γ.

Equation A-5 shows that s is maximal at the surface of the membrane: $s_{max} = s(0)$ or

$$s_{max} = \left(\frac{3\gamma}{2}\right)^{1/3} \qquad [A\text{-}6]$$

We see that $s_{max} \sim K_c^{1/3}$. The dependence on the porosity and permeability of the backing layer is even weaker: $s_{max} \sim (\varepsilon k_l^0)^{-1/6}$. The only parameter which almost linearly scales s_{max} is the backing layer thickness: $s_{max} \sim (l_b)^{2/3}$. Note that s_{max} is small if $\gamma \leqslant 10^{-3}$; this inequality establishes the limits of validity of Eq. A-5 and A-6.

The cube root dependence of s_{max} on γ explains the difference in the results of Refs. 14,18,19,27. The effective parameter γ in Ref. 18 and 19 is four orders of magnitude larger than that in Ref. 14 and 27. This leads to a roughly 10 times larger maximal saturation in Ref. 18 and 19, as compared to that in Ref. 14 and 27.

Equation A-5 predicts the existence of a "boundary layer," a region with a large gradient of saturation at $\tilde{x} = 1$ (Fig. A-1). We define the width of the boundary layer $\tilde{\delta}$ as $\tilde{\delta} = 1 - \tilde{x}_{1/2}$; $\tilde{x}_{1/2}$ is a point where the saturation reaches half of its maximum: $s(\tilde{x}_{1/2}) = s_{max}/2$. Equating $(3\gamma(1-\tilde{x}_{1/2}^2)/2)^{1/3} = \frac{1}{2}(3\gamma/2)^{1/3}$, we get

$$\tilde{\delta} = 1 - \sqrt{\frac{7}{8}} \qquad [A\text{-}7]$$

or $\tilde{\delta} \simeq 0.0646$. Essentially, $\tilde{\delta}$ does not depend on γ and is thus a universal value. A strong variation of saturation hence occurs in a 6.5% boundary layer at the cathode backing layer/channel interface; in the rest of the backing layer, the saturation is nearly constant. Note that this is true if the variation of c_w across the backing layer is not large.

Qualitatively similar profiles of saturation were obtained in Ref. 49 for the case when liquid water is generated in the electrochemical reaction and condensation/evaporation are negligible. Inspection of the numerical profiles $s(x)$ presented in Ref. 49 shows that these profiles also exhibit a 6.5% boundary layer. It is easy to show that the model of Ref. 49 leads to Eq. A-4 with a nonzero left boundary condition $\partial s/\partial\tilde{x}|_{\tilde{x}=0} = -a^2$, where a^2 is a function of the local current density. However, this boundary condition has a minor effect on the shape of the solution in the boundary layer. In other words, regardless of the physical origin of the source of liquid water the thickness of the boundary layer is determined by the transport term $\partial/\partial x(D_s\partial s/\partial x)$, which in Ref. 49 is similar to ours.

List of Symbols

b	Tafel slope, V
b_{app}	apparent Tafel slope, V
c	total molar concentration of the mixture, mol cm^{-3}
$c^0_{O_2}$	inlet oxygen concentration, mol cm^{-3}
c_{O_2}	local oxygen molar concentration in the channel, mol cm^{-3}
$c_{O_{2ref}}$	reference oxygen molar concentration, mol cm^{-3}
$c_{H_{2ref}}$	reference hydrogen molar concentration, mol cm^{-3}
c_{H^+}	proton molar concentration in membrane, mol cm^{-3}
c_w	molar concentration of water vapor, mol cm^{-3}
c_l	molar concentration of liquid water in membrane phase, mol cm^{-3}
c_w^{sat}	molar concentration of saturated water vapor, mol cm^{-3}
D_i	effective diffusion coefficient of ith gas component, cm^{-2} s^{-1}
D_i^B	binary diffusion coefficient of ith gas component, cm^{-2} s^{-1}
D_i^K	Knudsen diffusion coefficient of ith gas component, cm^{-2} s^{-1}
D_{O_2}	effective diffusion coefficient of oxygen in the backing layer, cm^{-2} s^{-1}
$D^{dry}_{O_2}$	oxygen diffusion coefficient in dry backing layer, cm^{-2} s^{-1}
$D^{Q2D}_{O_2}$	effective oxygen diffusion coefficient resulting from analytical quasi-2D model, cm^{-2} s^{-1}
$D^{Q3D}_{O_2}$	effective diffusion coefficient of oxygen, resulting from Q3D model, cm^{-2} s^{-1}
D_s	effective diffusion coefficient of liquid saturation, cm^{-2} s^{-1}
D_l	diffusion coefficient of liquid water in membrane, cm^{-2} s^{-1}
F	Faraday constant, 9.6495×10^4 C mol^{-1}
f_λ	function Eq. 5
h	channel height, cm
i^*	exchange current density per unit volume, A cm^{-3}
j	local current density, A cm^{-2}
$\bar{j}$	mean current density in a cell, A cm^{-2}
j_D	limiting current density due to imperfect oxygen diffusion in the backing layer, A cm^{-2}
j_m	proton current density in membrane, A cm^{-2}
j_*	characteristic current density, A cm^{-2}
k	dimensionless parameter
K_c	frequency of condensation, s^{-1}
K_e	frequency of evaporation, s^{-1}
l_t	thickness of the catalyst layer, cm
l_b	thickness of the backing layer, cm
l_m	thickness of the membrane, cm
M	molecular weight, g mol^{-1}
N	molar flux, mol cm^{-2} s^{-1}
n	number of electrons participating in the reaction ($n = 4$)
n_d	drag coefficient
p_c	capillary pressure, g cm^{-1} s^{-2}
p_g	gaseous pressure, g cm^{-1} s^{-2}
p_l	liquid pressure, g cm^{-1} s^{-2}
$Q_{a,c}$	rate of electrochemical reaction, A cm^{-3}
$\bar{r}$	mean pore radius in the catalyst layer, cm
R	cell resistance, Ω cm^2
R_l^{ec}	molar rate of liquid water evaporation or water vapor condensation, mol cm^{-3} s^{-1}
R_l^{ORR}	molar rate of liquid water production in ORR, mol cm^{-3} s^{-1}
R_n	contact resistance, Ω cm^2
R_m	membrane resistance, Ω cm^2
s	liquid saturation
S_i	stoichiometry coefficient of ith component
T	cell temperature, K
V_{oc}	cell open-circuit voltage, V
$v(z)$	flow velocity, cm s^{-1}
v_ℓ	velocity of liquid water in the backing layer, cm s^{-1}
x	coordinate across the cell, cm
y	coordinate along the cell surface Fig. 1, cm
z	coordinate along the channel, cm

Greek

α	transfer coefficient
γ	dimensionless parameter
ε	porosity of backing layer
ε_m	volume fraction of membrane in the catalyst layer
η	polarization voltage, V
ζ	membrane water content (number of water molecules per SO_3^- group)
λ	stoichiometry ratio of oxygen flow
Λ	water sorption isotherm of membrane
μ_l	viscosity of liquid water, g cm^{-1} s^{-1}
ξ_i	molar fraction of ith component
ρ^0	density of the flow in the channel, g cm^{-3}
ρ_l	density of liquid water, g cm^{-3}
$\sigma_{a,c}$	electron conductivity of the carbon phase, Ω^{-1} cm^{-1}
σ_t	proton conductivity of the catalyst layer, Ω^{-1} cm^{-1}
σ_m	bulk membrane conductivity Ω^{-1} cm^{-1}
ϕ	matching function (Eq. 3)
ψ	porosity of the catalyst layer

Subscripts

0	value at the channel inlet (at $z = 0$)
b	in the backing layer
h	in the channel
m	in the bulk membrane
t	in the catalyst layer

References

1. T. E. Springer, T. A. Zawodzinski, and S. Gottesfeld, *J. Electrochem. Soc.*, **138**, 2334 (1991).
2. D. M. Bernardi and M. W. Verbrugge, *AIChE J.*, **37**, 1151 (1991).
3. D. M. Bernardi and M. W. Verbrugge, *J. Electrochem. Soc.*, **139**, 2477 (1992).
4. D. Bevers, M. Wöhr, K. Yasuda, and K. Oguro, *J. Appl. Electrochem.*, **27**, 1254

(1997).
5. L. You and H. Liu, *Int. J. Hydrogen Energy*, **26**, 991 (2001).
6. L. Pisani, G. Murgia, M. Valentini, and B. D. D'Aguanno, *J. Electrochem. Soc.*, **149**, A898 (2002).
7. T. F. Fuller and J. Newman, *J. Electrochem. Soc.*, **140**, 1218 (1993).
8. T. V. Nguyen and R. E. White, *J. Electrochem. Soc.*, **140**, 2178 (1993).
9. J. S. Yi and T. V. Nguyen, *J. Electrochem. Soc.*, **145**, 1149 (1998).
10. A. A. Kulikovsky, J. Divisek, and A. A. Kornyshev, *J. Electrochem. Soc.*, **146**, 3981 (1999).
11. A. A. Kulikovsky, J. Divisek, and A. A. Kornyshev, *J. Electrochem. Soc.*, **147**, 953 (2000).
12. K. Dannenberg, P. Ekdunge, and G. Lindbergh, *J. Appl. Electrochem.*, **30**, 1377 (2000).
13. S. Um, C.-Y. Wang, and K. S. Chen, *J. Electrochem. Soc.*, **147**, 4485 (2000).
14. Z. H. Wang, C. Y. Wang, and K. S. Chen, *J. Power Sources*, **94**, 40 (2001).
15. L. You and H. Liu, *Int. J. Heat Mass Transfer*, **45**, 2277 (2002).
16. P. Futerko and I.-M. Hsing, *Electrochim. Acta*, **45**, 1741 (2000).
17. I.-M. Hsing and P. Futerko, *Chem. Eng. Sci.*, **55**, 4209 (2000).
18. W. He, J. S. Yi, and T. V. Nguyen, *AIChE J.*, **46**, 2053 (2000).
19. D. Natarajan and T. V. Nguyen, *J. Electrochem. Soc.*, **148**, A1324 (2001).
20. R. Bradean, K. Promislow, and B. R. Wetton, *Numer. Heat Transfer, Part A*, **42**, 121 (2002).
21. J. M. Stockie, K. Promislow, and B. R. Wetton, *Int. J. Numer. Methods Fluids*, **41**, 577 (2003).
22. P. Berg, K. Promislow, J. St. Pierre, J. Stumper, and B. Wetton, *J. Electrochem. Soc.*, **151**, A341 (2004).
23. S. Dutta, S. Shimpalee, and J. W. Van Zee, *J. Appl. Electrochem.*, **30**, 135 (2000).
24. S. Shimpalee and S. Dutta, *Numer. Heat Transfer, Part A*, **38**, 111 (2000).
25. W.-K. Lee, S. Shimpalee, and J. W. Van Zee, *J. Electrochem. Soc.*, **150**, A341 (2003).
26. T. Zhou and H. T. Liu, *Inst. Transp. Eng. J.*, **3**, 177 (2001).
27. T. Berning and N. Djilali, *J. Electrochem. Soc.*, **150**, A1598 (2003).
28. H. Meng and C. Y. Wang, *Chem. Eng. Sci.*, **59**, 3331 (2004).
29. J. Kim, S.-M. Lee, S. Srinivasan, and Ch. E. Chamberlin, *J. Electrochem. Soc.*, **142**, 2670 (1995).
30. J. H. Lee, T. R. Lalk, and A. J. Appleby, *J. Power Sources*, **70**, 258 (1998).
31. G. Squadrito, G. Maggio, E. Passalacqua, F. Lufrano, and A. Patti, *J. Appl. Electrochem.*, **29**, 1449 (1999).
32. R. F. Mann, J. C. Amphlett, M. A. I. Hooper, H. M. Jensen, B. A. Peppley, and P. R. Roberge, *J. Power Sources*, **86**, 173 (2000).
33. L. Pisani, G. Murgia, M. Valentini, and B. D'Aguanno, *J. Power Sources*, **108**, 192 (2002).
34. A. A. Kulikovsky, *Electrochem. Commun.*, **4**, 845 (2002).
35. A. A. Kulikovsky, *Electrochim. Acta*, **49**, 617 (2004).
36. A. A. Kulikovsky, *Electrochem. Commun.*, **4**, 318 (2002).
37. R. B. Bird, W. E. Stewart, and E. N. Lightfoot, *Transport Phenomena*, Wiley, New York (1960).
38. M. C. Leverett, *Trans. Am. Inst. Min., Metall. Pet. Eng.*, **142**, 152 (1941).
39. K. S. Udell, *Int. J. Heat Mass Transfer*, **28**, 485 (1985).
40. A. A. Kulikovsky, *Fuel Cells*, **1**, 162 (2001).
41. A. A. Kulikovsky, *J. Electrochem. Soc.*, **150**, A1432 (2003).
42. J. T. Hinatsu, M. Mizuhata, and H. Takenaka, *J. Electrochem. Soc.*, **141**, 1493 (1994).
43. A. A. Kulikovsky, *Electrochem. Commun.*, **3**, 572 (2001).
44. D. L. Scharfetter and D. L. Gummel, *IEEE Trans. Electron Devices*, **ED-16**, 64 (1969).
45. A. A. Kulikovsky, *J. Comput. Phys.*, **173**, 716 (2001).
46. T. J. VanderNoot and I. Abrahams, *J. Electroanal. Chem.*, **448**, 17 (1998).
47. A. A. Kulikovsky, *Electrochim. Acta*, **49**, 5187 (2004).
48. A. A. Kulikovsky, *Electrochem. Commun.*, **6**, 969 (2004).
49. U. Pasaogullari and C. Y. Wang, *J. Electrochem. Soc.*, **151**, A399 (2004).